

## 3 | Metal/Non-Metal Loaded/Doped $g\text{-C}_3\text{N}_4$ Monolayer

---

*To improve the photocatalytic activity of CN, an efficient method of loading metal (Co/Fe/Ag) and doping non-metal (B/O/P) jointly has been addressed in this chapter. The electronic characteristics of the pristine and functionalized CN with loading and doping together have been analyzed. Based on band edges, the Co and B co-doping has been screened as a candidate for overall photocatalytic water splitting and highlights the synergistic effects of B-doping and Co-loading in CN in terms of the formation of impurity states, high visible light absorption, charge redistribution, and lower OER and HER overpotential along with suitable redox potentials.*

---

### 3.1 Loaded/Doped $g\text{-C}_3\text{N}_4$

Our efficient utilization of renewable energy resources is guided by the requirements of the current scenario. A wealth of solar energy, our understanding of the impending energy crisis, and our quest for materials free of hazards have all encouraged us to investigate effective, affordable, and environmentally benign photocatalyst materials that are well-suited to the task of fixing future energy issues. The process of converting graphite into thin layers created several opportunities for the low-dimensional use of other materials. The scientific community has recently given a great deal of attention to several 2D-sheet structures due to their unique features and simple production methods. Many 2D-sheet materials have previously been thoroughly investigated, including graphene, molybdenum disulfide, graphitic carbon nitride ( $CN$ ), hexagonal boron nitride, and manganese dioxide [77–79]. Materials with potential photocatalytic capabilities must be checked for band gap compatibility with the visible light spectrum. Additionally, materials plentiful in nature and less harmful to living things must be selected.  $CN$  has been extensively explored due to its favorable band gap of 2.70 eV [80–82], which has demonstrated excellent electrical and optical characteristics.  $CN$  is regarded as a potential metal-free photocatalyst for several photocatalytic redox processes, including oxidative dehydrogenation of amines, organic pollutant degradation, and water splitting. It has high chemical and thermal stability. Its practical uses, which include small surface area, low visible light responsiveness, and quick photogenerated  $e^-h^+$  pair recombination, have been limited by the drawbacks in the bulk form of  $CN$ .

Numerous techniques, including the doping of metal and non-metal atoms, semiconductor compositing, noble metal depositing, nanostructure engineering, and semiconductor doping, have been demonstrated to increase the photocatalytic capacity of  $CN$  in recent years. For increased intrinsic photo-absorption,  $CN$  nanosheets are described, and the photoluminescence quantum yield has increased to 19.6%. Due to changes in the topology and relationship pattern of  $CN$  sheets, [83] interstitial doping of non-metals such as S and P increased the absorption

in the visible energy region [24]. The HOMO and LUMO of H-, B-, O-, S-, F-, and As-doped  $CN$  efficiently separated the photogenerated  $e^-h^+$  pairs and improved the photocatalytic effectiveness, according to research by Lu et al. [84]. By substituting the C atom in the ring, B-doping increased the visible-light sensitivity of  $CN$  and also created impurity states close to the VBM. The lifespan of photogenerated charge carriers was extended by B-doping in  $CN$ , which is advantageous for boosting photocatalytic activity for  $H_2$  evolution and  $CO_2$  conversion [85, 86]. Whereas Fe and Ni loaded on  $CN$  penetrated the void present and extended the charge carrier migration distance, which suppressed the recombination of  $e^- - h^+$  pairs, Cu and Zn contributed to inter-layer charge carrier migration [25]. Co-doped  $CN$  has enhanced the photocatalytic properties due to the formation of Co-N bonds and has also been reported as promising catalysts in the photo-assisted degradation of sulfate radical-based organic materials [87]. By reducing the band-gap or forming gap states, Ling et al. [88] have performed S atom doping or C/N vacancy in  $CN$  and observed an improvement in light responsiveness. Meanwhile, the coupling effect at the  $g - C_3N_4/MoS_2$  interface by controlling the band edge potentials of  $CN$  Using hybrid density functional theory (h-DFT), Zhao et al. [89] have investigated the photocatalytic mechanism of an F and Ti co-doped heptazine-based  $CN$  heterostructure.

The high oxidation overpotential of 1.56 eV in  $CN$  has been addressed in several ways [82], by various doping, loading, and heterostructure generation. Our focus was drawn to the functionalization of  $CN$  with non-metal doping and TM loading due to a lack of research on the synergistic effects of these two approaches. Selecting a non-metal and TM photocatalyst that is efficient is crucial, considering the inherent characters of the B/P/O-non-metal and Co/Ag/Fe doping and loading [7, 24, 90] over the  $CN$ -structure these adatoms and their combination are considered for the overall water-splitting capabilities. The current work concentrated on the thermodynamical investigations of water splitting processes (HER and OER) and TM (Co/Ag/Fe)-loaded and NM (B/P/O)-doped  $CN$  utilizing DFT. Based on band edges they are screened for reduction and oxidation potential straddling. Thereafter the suitable catalysts have been studied in terms of band gap reduction,

enhancement in visible light absorption, charge redistribution, and separation. In the current investigation, two alternative locations for NM doping were taken into consideration, and the TM atom was inserted in the void of  $CN$ . For TM and NM, two distinct interaction situations (short- and long-range) were examined.

## 3.2 Computational Methods

DFT as implemented in the Quantum Espresso software was used to investigate structural, electronic, optical, and thermodynamic characteristics. The software packages VESTA, XCrySDen [91], and BURAI were utilized for structural design and visualization. The GGA of Perdew et al.[58], known as PBE-GGA, was used to calculate the optical and thermodynamic properties, structural optimization, and energy band structure. The hybrid functional HSE06 [58, 60] was only taken into consideration for the calculation of the density of states (DOS), which yields a better energy gap value than the PBE-GGA calculation. We have taken into account ultra-soft pseudo-potentials (USPP) for structural, and electronic properties, and norm-conserving pseudo-potentials (ONCV) for optical properties. Using the Grimme-D2 [70] technique, total energies were adjusted for the vdW interaction. For all the computations, a  $5 \times 5 \times 1$  Monkhorst-Pack k-point grid was utilized. Plane waves-based basis sets, which have a maximum kinetic energy of 540 and 60 Ry, respectively, are used to represent charge densities and the Kohn-Sham orbitals. These basis sets were identified by observing the convergence of the total energy with the increase in plane wave kinetic energy. The fixed convergence threshold was  $10^{-6}$  a.u. Through quasi-Newton ionic relaxation and the use of the Broyden, Fletcher, Goldfarb, Shanno (BFGS) method [92–95], structural parameters were improved.

### 3.2.1 Structural Model

The most stable form of  $C_3N_4$  among all the other forms is said to be hexagonal heptazine-based  $CN$ . Here, we generated a unit cell of heptazine  $CN$ , with a radius of 2.38 Å for the void and 1.18 Å for the pore, with a lattice parameter of 7.14 Å. We extended the cell in both the x and y directions, resulting in a  $2 \times 2 \times 1$  supercell, this supercell generates the monolayer of  $CN$ . With a vacuum of 15 Å, the cell is extended in the Z-direction, which was determined to be the most suitable vacuum size after considering different vacuum sizes based on saturation in total energy to prevent interaction with the next periodic layer. As seen in Fig. 3.1, the 56 atoms in this supercell are made up of 24 C and 32 N atoms. At the bay ( $C^{bay}$ ) or corner ( $C^{cor}$ ) sites, a single C atom was replaced with an NM-atom, resulting in 4.16% doping at the C site, known as  $NM_{int}-CN$  and  $NM_{non-int}-CN$ , respectively. In the void space of  $CN$ , one TM atom with a concentration of 1.78% (called  $TM-CN$ ) was implanted. We have examined two NM-doping sites (at  $C^{bay}$  and  $C^{cor}$ ) with TM-loading for loading and doping together, resulting in two distinct structures that we will refer to as  $(TM - NM)_{int}-CN$  and  $(TM - NM)_{non-int}-CN$ , respectively. We have determined the bonding energy ( $\Delta E_b$ ) for structural stability in all systems under loading, doping, and both utilizing:

$$\Delta E_b = E_{CN_{TM-NM}} - (E_{CN} + \mu_{TM} + \mu_{NM} - \mu_C) \quad (3.1)$$

Where  $\mu_{TM}, \mu_{NM}, \mu_C$  indicates the chemical potential of TM, NM, and C determined from their bulk or compound form, and  $E_{CN_{TM-NM}}$  and  $E_{CN}$  represent the total energy of loading/doping and pristine samples, respectively. Since the periodicity and smaller size of the doping and loading atoms offer a comparable chemical environment to that of the supercell, the adsorption of the intermediate across the surface was carried out on the unit cell for thermodynamic characteristics.

The adsorption energy ( $\Delta E_{ads}$ ) for any adsorbate species over the substrate surface is calculated as the energy difference

$$\Delta E_{ads} = E_{sub+A} - (E_{sub} + E_A) \quad (3.2)$$

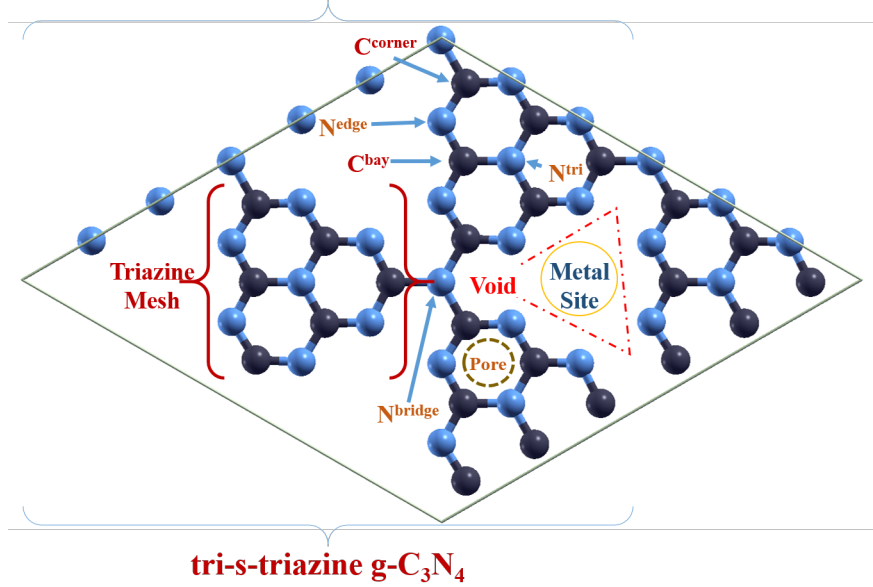


FIGURE 3.1: Pristine structure with  $N^{edge}$ ,  $N^{tri}$ ,  $N^{bridge}$ ,  $C^{cor}$ ,  $N^{bay}$ , triazine-mesh, void, and pore for  $CN$  tri-s-triazine form.

where the total energy of "substrate + adsorbate," substrate, and adsorbate are indicated by the values  $E_{sub+A}$ ,  $E_{sub}$ , and  $E_A$ , respectively. The same computational parameters were used for each of the included species to eliminate errors.

### 3.3 Structural and Electronic Properties

The crystal structure of a monolayer of  $CN$  with five substitutional doping sites  $N^{edge}$ ,  $N^{tri}$ ,  $N^{bridge}$ ,  $N^{bay}$ , and  $C^{cor}$  are illustrated in Fig. 3.1. In this case,  $N^{bridge}$  connects three s-triazine molecules,  $N^{edge}$  represents a tri-bonded N at the mesh's center, and  $N^{tri}$  represents a double-bonded atom at the mesh's edge. Triple-bonded atoms  $C^{bay}$  and  $C^{cor}$  are located at the corner and bay sites, respectively, of the matrix. In the current computations, the (Co/Ag/Fe) atom has been loaded at the "Metal Site" void in Fig. 3.1. Multiple sites were examined for stability in (B/P/O)-doping. Because of the electronegative character of N, the C atom was determined to be the most stable site when it came to substitutional doping of the B/P/O-atom. We have examined both the  $C^{bay}$  and  $C^{cor}$  sites among the various C-sites for B/O/P-doping, for both the sites negative  $E_{ads}$  verify the stability of sample formation. To screen the most suitable system and to further

TABLE 3.1: The theoretical values of  $E_{VB}$  eV, and  $E_{CB}$  eV for all the metal-non metal functionalized  $CN$

Sample	$E_{VB}$ eV	$E_{CB}$ eV
$CN$	1.65	-1.11
$B - CN$	1.19	-1.02
$Co - CN$	1.48	-0.80
$(Co - B)_{int} - CN$	1.38	-1.00
$(Co - B)_{non-int} - CN$	1.21	-0.93
$P - CN$	1.38	-0.42
$Ag - CN$	0.85	-0.79
$(Ag - P)_{C^{bay}} - CN$	1.03	-0.48
$(Ag - P)_{C^{cor}} - CN$	0.82	-0.38
$O - CN$	1.09	-1.15
$Fe - CN$	0.77	-0.67
$(Fe - O)_{C^{bay}} - CN$	-0.01	-0.67

study it elaborately from the perspective of structural, electronic, optical, and photocatalytic activity we have computed the stable systems for the band edges utilizing the HSE06 functional, as shown in Table. 3.1. These band edges were calculated using the DOS, here among all the systems tabulated, only  $(Co - B) - CN$  was seen to straddle the reduction-oxidation potential for the NHE scale. Therefore,  $(Co - B) - CN$  is screened in for further calculations.

An energy difference of 0.28 eV was computed for Co-loading with B-doping, and the  $C^{cor}$  site was found to be more stable energetically than the  $C^{bay}$  site.  $B_{int} - CN$ ,  $B_{non-int} - CN$ ,  $Co - CN$ ,  $(Co - B)_{int} - CN$ , and  $(Co - B)_{non-int} - CN$  have computed binding energies of -1.22, -1.57, 1.98, -0.63, and -0.35 eV. The negative value of this binding energy implies exothermic and spontaneous pathways, while the lower value of  $\Delta E_b$  indicates the easy integration of impurity atoms in the supercell. The optimized structures may be seen in Fig. 3.2, where the vdW interaction does not cause any distortion in the planer geometry (z-direction). After optimization, it is seen that the Co loading in the void causes it to be displaced towards the triangular void's corner, where it forms a connection with two of the N atoms on the edge. The optimized lattice parameter for  $CN$  was determined to be  $a = b = 14.25 \text{ \AA}$ , following the reported unit-cell lattice parameter. The functionalized  $CN$  was further calculated using this improved parameter.  $B_{int} - CN$  and  $B_{non-int} - CN$  yielded lattice parameters of  $a = b = 14.23$

$\text{\AA}$  and  $a = b = 14.30 \text{ \AA}$ , respectively.  $Co-CN$ ,  $B_{int}-CN$  and  $B_{non-int}-CN$  had computed lattice parameters of  $a = b = 14.22, 14.24,$  and  $14.31 \text{ \AA}$ , respectively. Fig. 3.3 displays the DOS for  $CN$ ,  $B_{int}-CN$ ,  $B_{non-int}-CN$ ,  $Co-CN$ ,  $(Co - B)_{int}-CN$ , and  $(Co - B)_{non-int}-CN$  that were examined using HSE06. The calculated band gap value for pristine  $CN$  is 2.76 eV, which is per the experimental values of 2.78 eV and 2.67 eV [6, 7].  $E_F$  is moved towards the VB in  $B_{int}-CN$  and  $B_{non-int}-CN$ , resulting in the formation of a p-type semiconductor, while the band gap is narrowed to 1.76 eV and 2.21 eV, respectively. In  $Co-CN$ ,  $E_F$  is moved toward the CB, suggesting that it is an n-type semiconductor, and a broad IB emerges in the forbidden band gap area of  $CN$ , suggesting the generation of deep levels for charge carriers. For  $CN$  partial charge compensation,  $E_F$  is displaced in the center of the band gap in  $(Co - B)_{int}-CN$  and  $(Co - B)_{non-int}-CN$ , suggesting a combination of B-doping and Co-loading. Together, Co-loading and B-doping generated filled impurity states that were physically distinct from the lower VB. The  $N^{edge}$ -2p states predominate in  $CN$  (Fig. 3.3a), whereas  $N^{tri}$ -2p and  $N^{bridge}$  and C-2p states hybridize to generate the CB. The contribution of N-2s orbitals, which is relatively modest in comparison to the 2p orbitals of N and C, is shown by the shaded DOS in Fig. 3.3a.  $B_{int}-CN$  and  $B_{non-int}-CN$ 's PDOS, shown in Fig. 3.3(b-c), indicate that  $E_F$  is shifting towards the VB and CB, primarily because of the impurity state of B-2p forming at 2.5 eV and 2.75 eV, respectively, while VB is made up of  $N^{edge}$ -2p states, which correspond to B's neighboring N atoms. The inclusion of B into  $CN$  causes the B-2p states to hybridize with the N-2p states. This results in changes to the C-2p and N-2p states in both CB and VB, which are mostly caused by the generation of new N-B bonds and the different interactions between the C-2p and N-2p states in the C-N bonds in the mesh. On the other hand, the generation of Co-3d impurity states between -2.5 and -1.5 eV above the VB zone is seen for  $Co-CN$  (Fig. 3.3d). In this region, there are also minor isolated DOS of N-2p and C-2p states that are hybridizing with Co-3d states. Charge transfer, which will be covered in the following section, may be used to understand the hybridization between the Co-3d and N-2p states in CB. This hybridization indicates some direct or indirect interaction with

Co. Compared to  $Co\text{-CN}$ ,  $(Co - B)_{int}\text{-CN}$ 's isolated DOS between -1.5 and -0.75 eV sharpened, mostly because of the extra B-2p states in the same energy range (Fig. 3.3e). At the top of the VB, however, dominant isolated DOS were generated via orbital hybridization. In the VB and CB,  $E_F$  is moved between the hybridized intermediate states of Co-3d and B-2p. Higher absorption in the low-energy region may be caused by these impurity states, which may also serve as deep trapping sites for charge carriers. The generated impurity states for  $(Co - B)_{non-int}\text{-CN}$  (Fig. 3.3f) are broader than those for  $(Co - B)_{int}\text{-CN}$ .

The effective mass ratio ( $\beta = (m_e^*)/(m_h^*)$ , where  $m_e^*$  and  $m_h^*$  represent the effective masses of electron and hole, respectively), is a crucial parameter in determining the rate of recombination of  $e^- - h^+$  pairs. This process is also important in charge carrier separation. A greater variation in the  $e^- - h^+$  mobility and, consequently, a lower recombination rate, are indicated by an effective mass ratio bigger or smaller than one, which also indicates their availability for redox reactions over a longer time range and stronger photocatalytic activity. The band curvature average was taken into account for the effective mass calculations, but for the sample containing the IB, the transitions from VB to CB, VB to IB, and from IB to CB were assessed, and the average value was further examined as compiled in Table. 3.1. For  $CN$ ,  $B_{int}\text{-CN}$ , and  $B_{non-int}\text{-CN}$ , the value of  $m_e^*$  is computed as 1.55, 2.47, and 1.38  $m_e$  ( $m_e$  is the mass of free  $e^-$ ), with  $B_{non-int}\text{-CN}$  having the lowest value of  $m_e^*$  denoting the highest e-mobility. IB/impurity states are created for  $Co\text{-CN}$ ,  $(Co - B)_{int}\text{-CN}$ , and  $(Co - B)_{non-int}\text{-CN}$ , serving as a meta-stable level for charge carriers before their transition onto CB. These have the potential to serve as a trapping site to lower the  $e^- - h^+$  pair's recombination rate.  $(Co - B)_{int}\text{-CN}$  was found to have the lowest rate of charge carrier recombination in the impurity states when compared to  $Co\text{-CN}$  and  $(Co - B)_{non-int}\text{-CN}$ , indicating that  $(Co - B)_{int}\text{-CN}$  is the best appropriate material for charge carrier separation. This was shown by the highest value of  $\beta$ .

We have briefly analyzed the *Löwdin* charge transfer on each atom of the cell and charge transfer on a few selected atoms in the cell consisting of B and Co atoms

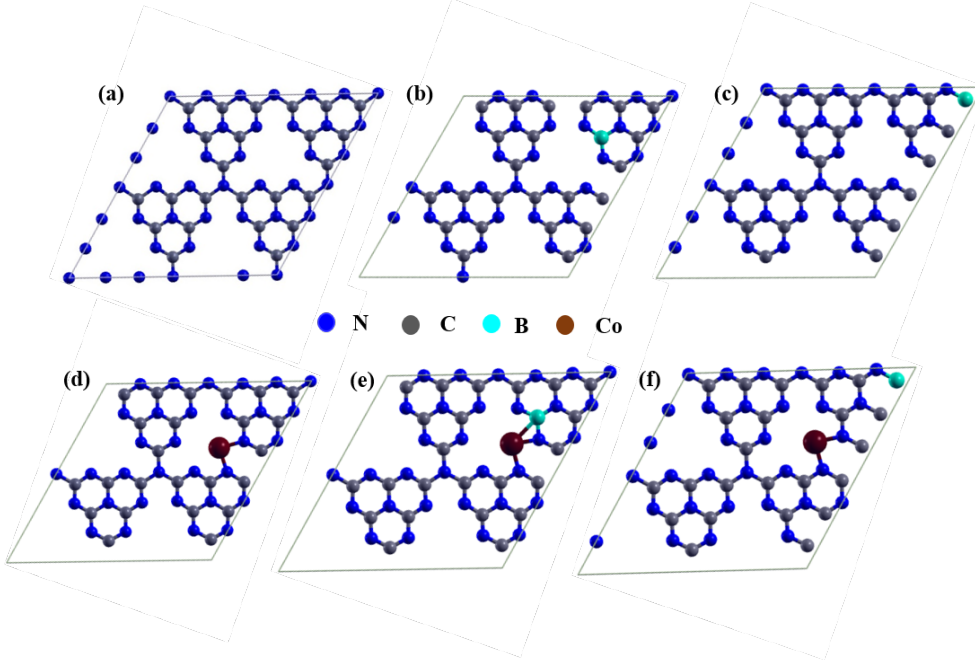


FIGURE 3.2: Optimized structure of (a) pristine  $CN$ , (b)  $B_{int-CN}$ , (c)  $B_{non-int-CN}$ , (d)  $Co-CN$ , (e)  $(Co-B)_{int-CN}$ , and (f)  $(Co-B)_{non-int-CN}$ .

TABLE 3.2: The theoretical values of  $E_F$ ,  $E_{vac}$ ,  $\Phi$ ,  $E_{BGC}$ , and  $\beta$  for  $CN$ ,  $B_{int-CN}$ ,  $B_{non-int-CN}$ ,  $Co-CN$ ,  $(Co-B)_{int-CN}$ , and  $(Co-B)_{non-int-CN}$

Sample	$E_F$ eV	$E_{vac}$ eV	$\Phi$ eV	$E_{BGC}$ eV	$\beta$
$CN$	-2.51	2.06	4.57	-4.69	0.49
$B_{int-CN}$	-3.44	2.06	5.49	-4.47	0.95
$B_{non-int-CN}$	-3.84	2.05	5.89	-4.66	0.72
$Co-CN$	-1.24	2.16	3.40	-4.64	1.99
$(Co-B)_{int-CN}$	-1.90	2.15	4.05	-4.62	2.71
$(Co-B)_{non-int-CN}$	-1.90	2.13	4.03	-4.57	1.55

as neighbors to study the effect of B-doping and Co-loading due to electronic charge in the  $CN$  monolayer.  $CN$  illustrates the transfer of charge from C to its neighboring N atoms, where  $N^{edge}$  atoms have a greater amount of negative charges than  $N^{tri}$  atoms. When compared to C atoms (in pristine  $CN$ ), B atoms share extra charge with nearby N atoms in  $B_{int-CN}$  and  $B_{non-int-CN}$ . Compared to  $N^{tri}$  ( $N^{bridge}$ ), nearby N atoms  $N^{edge}$  and  $N^{edge}$  ( $N^{edge}$ ) in  $B_{int-CN}$  ( $B_{non-int-CN}$ ) are more electronegative. In  $Co-CN$ , charge transfer from C to N and Co atoms is shown as a result of the development of a Co-N bond. Due to the transfer of charges among the nearby atoms, the Co atom receives an excess charge of 0.35e, which results in a total charge of 0.33e at the  $N^{edge}$  atom. The average charge

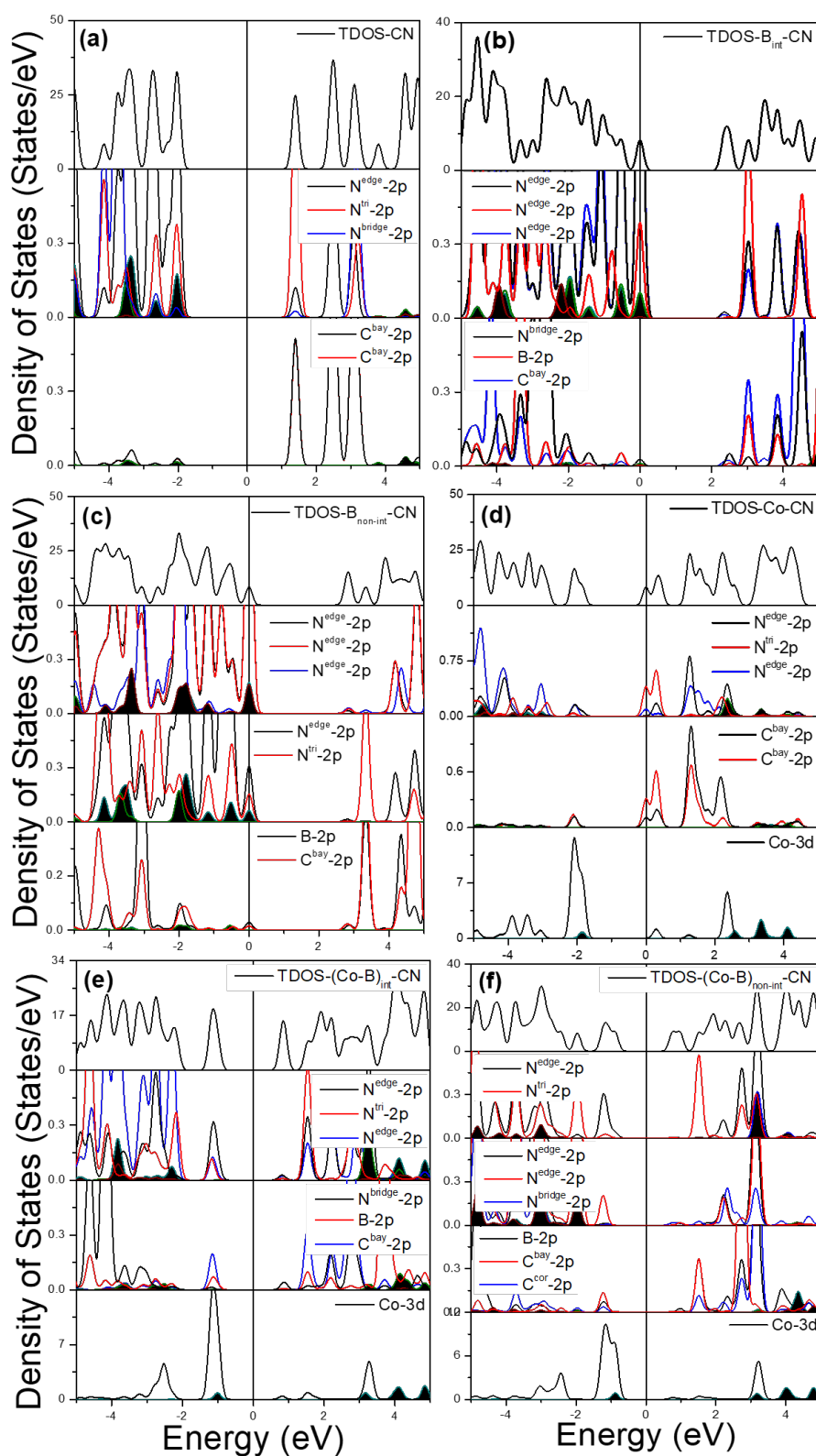


FIGURE 3.3: The PDOS for (a) pristine  $CN$ , (b)  $B_{int}CN$ , (c)  $B_{non-int}CN$ , (d)  $CoCN$ , (e)  $(Co-B)_{int}CN$ , and (f)  $(Co-B)_{non-int}CN$ . Zero energy is used to signify  $E_F$ . The corresponding atom's s-orbital is shown by the shaded region.

transfer from C and B atoms to  $N^{edge}$  [ $N^{edge}$ ] in  $(Co - B)_{int}\text{-CN}$  [ $(Co - B)_{non-int}\text{-CN}$ ] is 0.44e [0.36e], whereas it is 0.22e [0.23] to  $N^{tri}$  [ $N^{bridge}$ ]. For  $(Co - B)_{int}\text{-CN}$  and  $(Co - B)_{non-int}\text{-CN}$ , the charge transfer to the Co atom is 0.38e and 0.33e, respectively. Because of the existence of a Co atom in the void, there is a charge redistribution between B and  $N^{edge}$  atom through a channel of connecting atoms, which accounts for the difference in charge transfer between  $(Co - B)_{int}\text{-CN}$  and  $(Co - B)_{non-int}\text{-CN}$ .  $N^{edge}$  is the most electronegative atom in all of the studied CN monolayers because its charge gain for  $(Co - B)_{int}\text{-CN}$  is 0.47e and  $(Co - B)_{non-int}\text{-CN}$ 's charge gain is 0.36e (almost similar to 0.38e for  $N^{edge}$ ). It is also used as the adsorption site for water and intermediates for OER and HER. Cobalt Boride ( $CoB$ ,  $Co_2B$ , and  $Co_3B$ ) [96, 97] is an efficient electrocatalyst and has an effective interaction due to the partially filled 3d orbital of Co and 3p orbital of B with its effective electron affinity to give its single electron present in the 2p orbital to a relative more electronegative atom. This serves as inspiration for the formation of an electron channel through the redistribution of charges.

### 3.4 Optical and Photocatalytic Response

The theoretical band gap,  $E_{VB}$ , and  $E_{CB}$  for each of the monolayers under study are shown in Fig. 3.4a, together with the experimental band edges of the pristine CN bulk [6] and nano-sheet [7]. The band gap,  $E_{VB}$ , and  $E_{CB}$  values for the pristine film employing the PBE-GGA functional are also mentioned in Fig. 3.4. The functionalized CN monolayers'  $E_{CB}$  and  $E_{VB}$  analyses show that the  $E_{CB}$  is significantly above the reduction potential for hydrogen generation, whereas  $B_{int}\text{-CN}$  is far above the oxidation potential.  $B_{non-int}\text{-CN}$  and  $(Co - B)_{non-int}\text{-CN}$  are near the oxidation potential but do not cross it, while the remaining monolayers do. Therefore, CN,  $Co\text{-CN}$ , and  $(Co - B)_{int}\text{-CN}$  will be appropriate for the overall water splitting based on the band edge position analysis.

We have taken into consideration the complicated frequency-dependent dielectric function for the study of optical absorption, which gives us the absorbance and, imaginary component of the dielectric function. Fig. 3.4 depicts the average value

that may be inferred from the parallel and perpendicular components of the  $\alpha(\omega)$ .  $CN$  (the shaded region) exhibits two peaks of minimal absorption in the visible energy region. The characteristic peak in the UV region, at about 375 nm, displays the  $\pi - \pi^*$  transition, which is caused by charge transfer from  $CN$ 's populated VB of N-2p orbitals to CB of C-2p orbitals. Doping B at any level enhances absorption when compared to a pristine monolayer.  $Co-CN$ ,  $(Co - B)_{int-CN}$ , and  $(Co - B)_{non-int-CN}$ 's absorption spectra all show a comparable peak at 425, 460, and 500 nm, respectively, and their intensities match up with an increase in absorbance in the visible light spectrum. A peak at 3.35 eV for pristine  $CN$  can be seen from the imaginary component of the dielectric function displayed in Fig. 3.4b, which correlates to the intrinsic plasma frequencies. The electrical transition from the edge of the N-2p level in VB to the edge of the C-2p level in the CB is what gave rise to this peak. Two peaks are seen at 3.32(0.82), 3.32(0.85), 3.55(1.06), 3.34(0.89), and 3.55(0.85) eV in  $B_{int-CN}$ ,  $B_{non-int-CN}$ ,  $Co-CN$ ,  $(Co - B)_{int-CN}$ , and  $(Co - B)_{non-int-CN}$ . The electronic transition from the edge of the N-2p level in VB to the edge of the B-2p level around the  $E_F$  is responsible for the peak at 1.00 eV in  $B_{int-CN}$  and  $B_{non-int-CN}$ . The low energy peak is caused by the intra-band transition from the edge of the  $N^{tri}\text{-}2p$  level in the VB to the edge of the impurity Co-3d states for all three samples, while the peak around 3.50 eV is the result of the electronic transition from N-2p level in VB to  $C^{bay} - 2p$  level,  $N^{edge} - 2p$  level, and  $N^{edge} - 2p$  level in CB for  $Co-CN$ ,  $(Co - B)_{int-CN}$ , and  $(Co - B)_{non-int-CN}$ , respectively. The variation in the peak intensity and broadening is caused by the short and long-range interaction of the Co-B and corresponding charge redistribution among the planer atoms in  $CN$ . Consequently, the visible light absorption in  $(Co - B)_{int-CN}$  and  $(Co - B)_{non-int-CN}$  was enhanced by the production of IB as a result of Co loading and B-doping combined in  $CN$ 's forbidden band, which is advantageous to increase the photocatalytic activity. To function as a photocatalyst for the entire solar water splitting process, a semiconductor material must possess both a suitable band gap and a strong absorption of visible light. When producing hydrogen and oxygen from water, the location of the band edges is a crucial factor. When employing

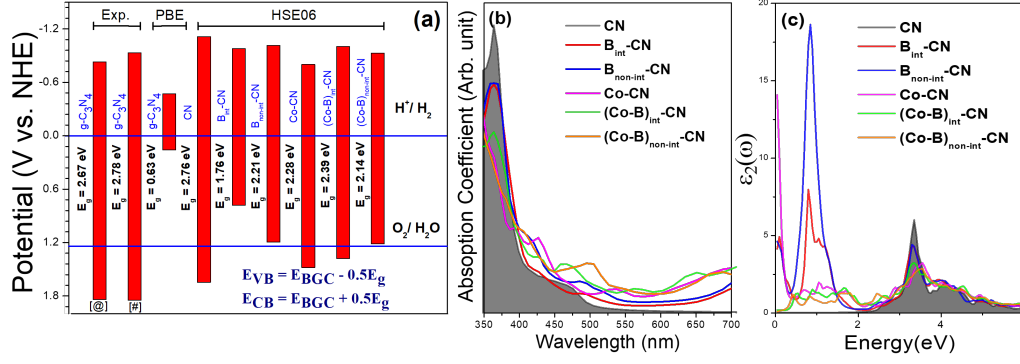


FIGURE 3.4: (a)  $E_{\text{VB}}$  and  $E_{\text{CB}}$  experimental values for bulk (@)[6] and nano-sheet(#)[7], together with band edges plot using various functional (PBE-GGA and HSE06), (b) Absorbance coefficient, and (c) imaginary part of dielectric function for  $\text{CN}$ ,  $B_{\text{int}}\text{-CN}$ ,  $B_{\text{non-int}}\text{-CN}$ ,  $\text{Co-CN}$ ,  $(\text{Co-B})_{\text{int}}\text{-CN}$ , and  $(\text{Co-B})_{\text{non-int}}\text{-CN}$ .

DFT under periodic boundary circumstances, the band edges should be positioned following the redox potential, which is a changeable factor depending on the usage of functional and pseudopotential. The estimated vacuum energies ( $E_{\text{vac}}$ ) from the analysis of the electrostatic potential profile are provided in Table. 3.2 together with the work function ( $\Phi$ ) and band gap center ( $E_{\text{BGC}}$ ) for each sample.

In addition to having a proper band gap, appropriate band edges for the NHE potential, charge carrier separation, and good optical performance in the visible energy range, effective photocatalysts also have to function well thermodynamically during OER and HER. We have looked at the reaction thermodynamics for both HER and OER in the section that follows.

### 3.4.1 Oxygen Evolution Reaction

The investigation of the adsorption of  $\text{H}_2\text{O}$ , OH, O, and OOH on the catalyst surface is crucial for understanding the water-splitting process. To do this, we looked at the adsorption energies of  $\text{H}_2\text{O}$ , OH, O, and OOH intermediate on both the pristine with all functionalized  $\text{CN}$ , and we used Eqs. 2.43, 2.44, 2.45, 2.46 to compute the adsorption energy of each. Based on the current charge redistribution study, we have taken into consideration the most electronegative N, or  $N^{\text{edge}}$ , in the current scenario for the adsorption of various intermediates.

Additionally, the same location is thought to be appropriate for water adsorption [98]. The water molecule's adsorption is initially investigated as the first of four electron steps. To do this, the water molecule is maintained at 3.42 Å above  $CN$ , with one O-H bond oriented toward the  $N^{edge}$  atom and another toward the plane of  $CN$ . The optimal structure following water adsorption demonstrates how the  $H_2O$  molecule changes orientation in each structure so that, as a result of N's electronegativity, the H atom forms a hydrogen bond with  $N^{edge}$ . Concerning  $CN$ , the value of  $\Delta E_{H_2O}$  of -0.43 eV agrees with the other theoretical report [98]. For  $B_{int}\text{-}CN$ ,  $B_{non-int}\text{-}CN$ ,  $Co\text{-}CN$ ,  $(Co - B)_{int}\text{-}CN$ , and  $(Co - B)_{non-int}\text{-}CN$ , the computed  $\Delta E_{H_2O}$  values are 0.04, -0.16, -0.14, 0.04, and -0.05 eV, respectively, suggesting the physical adsorption of water molecules since it requires little adsorption energy.

The adsorption energy ( $\Delta E_{OH^*}$ ), Gibbs free energy ( $\Delta G_1$ ), and the adsorbed state of  $OH^*$  on the catalyst's surface are crucial for the energy changes in upcoming reaction steps and the initial structure for the next step reaction. The water molecule on the catalyst's surface is converted to  $OH^*$  and  $(H^+ + e^-)$  pair according to the reaction in Eq. 2.34 as the first step of OER. Following calculation using  $OH^*$  as an intermediate, the structure results in the creation of O- $N^{edge}$  bonds for  $CN$ ,  $B_{int}\text{-}CN$ , and  $B_{non-int}\text{-}CN$ , and O- $N^{bridge}$  bonds, O-B bonds, and O-Co bonds for  $Co\text{-}CN$ ,  $(Co - B)_{int}\text{-}CN$ , and  $(Co - B)_{non-int}\text{-}CN$ , respectively, with additional distortion in the z plane and a change in orientation. For  $CN$ ,  $B_{int}\text{-}CN$ ,  $B_{non-int}\text{-}CN$ ,  $Co\text{-}CN$ ,  $(Co - B)_{int}\text{-}CN$ , and  $(Co - B)_{non-int}\text{-}CN$ , the computed values of  $\Delta E_{OH^*}$  are 2.15, 0.59, 0.74, -0.39, -0.23, and 0.03 eV, in that order.

Following the formation of  $O^*$  and  $(H^+ + e^-)$  pair formation due to the separation of a proton from the  $OH^*$  radical, as described by Eq. 2.35, the remaining  $O^*$  forms a bond with  $N^{edge}$  atoms for  $CN$ ,  $B_{int}\text{-}CN$ , and  $B_{non-int}\text{-}CN$ .  $Co\text{-}CN$ ,  $(Co - B)_{int}\text{-}CN$ , and  $(Co - B)_{non-int}\text{-}CN$  form bonds with  $N^{bridge}$ , Co & B, and Co; the corresponding  $\Delta E_{O^*}$  values are 2.51, 2.22, 2.62, 0.74, 1.46, and 1.45 eV, respectively. Thirdly, a second water molecule is converted to  $OOH^*$  and a  $(H^+ + e^-)$  pair by forming  $OH^*$ , which then combines with  $O^*$  as per Eq. 2.36.

OOH\* is adsorbed on the  $N^{edge}$  atom for  $CN$ ,  $B_{int-CN}$ , and  $B_{non-int-CN}$ , on the  $N^{bridge}$  atom for  $Co-CN$ , and on Co for  $(Co-B)_{int-CN}$ , and  $(Co-B)_{non-int-CN}$ . The  $\Delta E_{OOH^*}$  is 4.45, 4.32, 4.78, 3.40, 3.62, and 3.41 eV, respectively. OOH\* is changed into a pair of  $O_2$  and  $(H^+ + e^-)$  in the fourth reaction, whereas Eq. 2.37 determines the  $\Delta G_4$  of the final reaction to maintain the  $\Delta G_{1-4} = 4.92$  eV. Given that  $\Delta G_3$  is the highest value for every monolayer under study, it is regarded as the rate-determining step and must be taken into account when calculating the overpotential. Fig. 3.5 (a-f) shows the variance in  $\Delta G$  for pristine and functionalized  $CN$  at three distinct potentials:  $U = 0, 1.23,$  and  $\eta^{OER}+1.23$  V. This variation is determined using the change in adsorption energy with each intermediate. Using Eq. 2.50, the value of  $\eta^{OER}+1.23$  is determined as 3.55 V based on the observation that, for  $CN$ ,  $\Delta G_3 = 3.55$  eV is greatest at 0 V compared to the free energy changes of other reactions (Fig. 3.5). The free energy value decreased to 1.23 eV and the  $\eta^{OER}$  became 2.32 V at the equilibrium position at  $U = 1.23$  V. As a result, the figure at  $U = 3.55$  V represents the whole downhill OER process.  $B_{int-CN}$ ,  $B_{non-int-CN}$ ,  $Co-CN$ ,  $(Co-B)_{int-CN}$ , and  $(Co-B)_{non-int-CN}$  have  $\Delta G_3$  values of 2.45, 2.50, 3.01, 2.51 and 2.31 eV, respectively, at  $U = 0$  V. For  $U = 1.23$  eV, their corresponding values are reduced to 1.22, 1.20, 1.78, 1.28 and 1.08 V, which also corresponds to the respective  $\eta^{OER}$  values. The downhill nature of the reactions at  $U = \eta^{OER}+1.23$  suggests that they will occur concurrently. Every sample has a  $\eta^{OER}$  lower than the pristine  $CN$ , which helps to increase  $CN$ 's photocatalytic activity and is also in line with Wirth et al.[82]'s prediction.

Since  $CN$  has significant overpotentials, as was previously indicated, the position of  $E_{CB}/E_{VB}$  crossing the reduction/oxidation potential does not ensure the overall water splitting. Instead, the value of  $\eta^{OER}+1.23$  should be lower than the  $E_{VB}$ . The analysis of water oxidation efficiency in this example involves comparing  $\eta^{OER}+1.23$  with  $E_{VB}$ . All of the samples, except  $(Co-B)_{int-CN}$  and  $(Co-B)_{non-int-CN}$ , had lower  $E_{VB}$  than the corresponding  $\eta^{OER}+1.23$  value.  $(Co-B)_{int-CN}$  was determined to be the most appropriate material for the oxidation reaction out of all the samples, whereas  $(Co-B)_{non-int-CN}$  did not

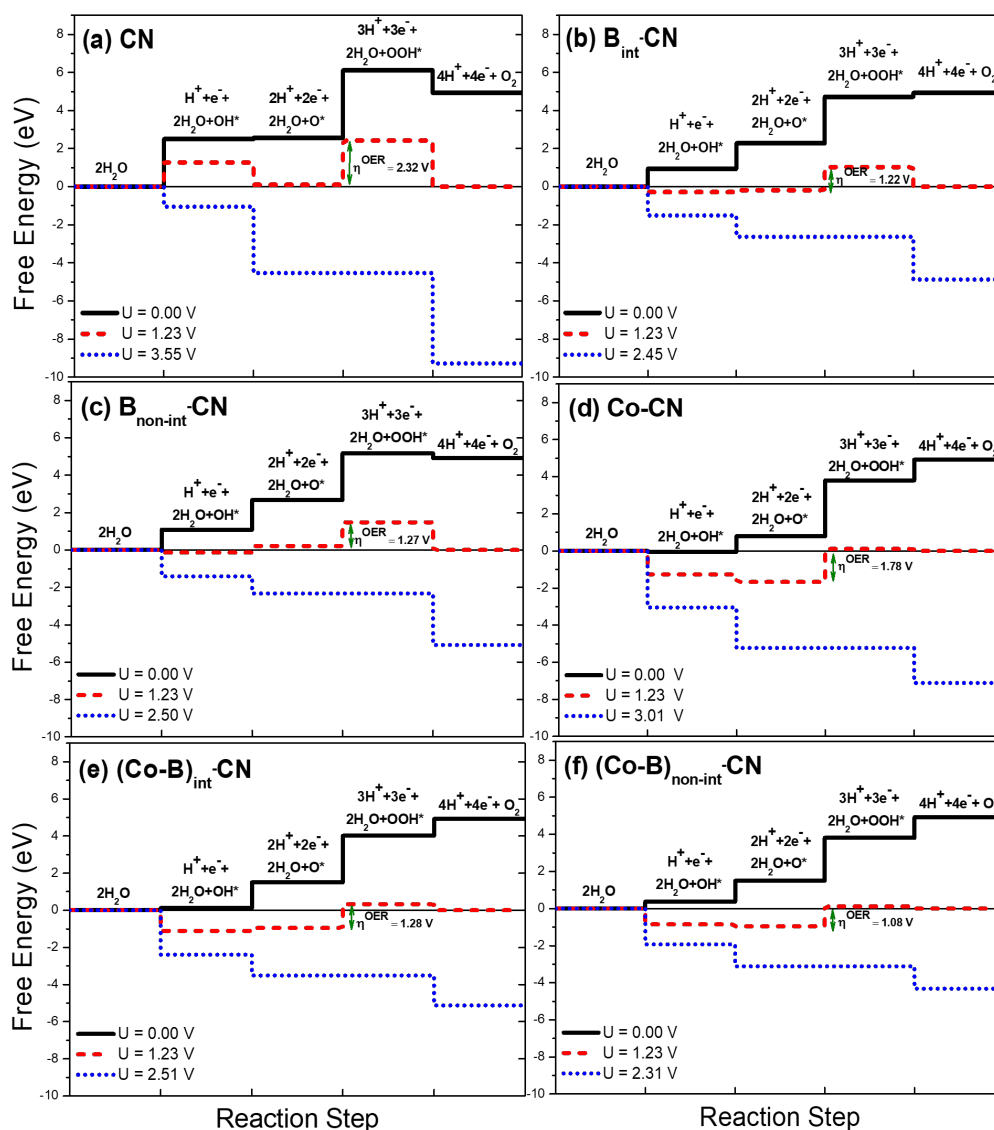


FIGURE 3.5: The Gibbs free energy plot for OER over (a) pristine  $CN$ , (b)  $B_{int}\text{-}CN$ , (c)  $B_{non-int}\text{-}CN$ , (d)  $Co\text{-}CN$ , (e)  $(Co\text{-}B)_{int}\text{-}CN$ , and (f)  $(Co\text{-}B)_{non-int}\text{-}CN$ .

cross the oxidative potential.

### 3.4.2 Hydrogen Evolution Reaction

Due to the strong electronegative character of the  $N^{edge}$  atom, an isolated H atom or  $H_3O$  molecule (for the effect of an additional water molecule) is adsorbed over it for HER (per Eqs. 2.38, 2.39, 2.40, 2.41). The adsorption energy is estimated

using Eq. 2.47 for H and Eq. 2.48 for  $H_3O$  molecule. For  $CN$  and  $(Co - B)_{int}\text{-}CN$ , the H atom forms a chemical link with the  $N^{edge}$  atom, however for  $B_{non-int}\text{-}CN$ , the increased electronegativity causes it to form a bond with  $N^{edge}$ .  $Co\text{-}CN$ ,  $(Co - B)_{int}\text{-}CN$ , and  $(Co - B)_{non-int}\text{-}CN$  exhibit a chemical connection between the H atom and Co. When it comes to the  $H_3O$  molecule, the H atom forms a hydrogen bond with  $N^{edge}$  in  $CN$ , while the  $H_2O$  molecule stays free. In  $(Co - B)_{int}\text{-}CN$ ,  $B_{non-int}\text{-}CN$ , and  $Co\text{-}CN$ , the H atom forms chemical bonds with  $N^{edge}$ ,  $N^{edge}$ , and Co, respectively. Fig. 3.6 displays the equivalent change in Gibbs free energy of the H atom and  $H_3O$  molecule ( $\Delta G_{H^*}$  and  $\Delta G_{H_3O^*}$ ). The favorable adsorption site is shown by the positive and negative values of the free energy, whereas the favorable adsorption site is implied by the negative value. For  $CN$ ,  $(Co - B)_{int}\text{-}CN$ , and  $(Co - B)_{non-int}\text{-}CN$ ,  $\Delta G_{H^*}$  and  $\Delta G_{H_3O^*}$  are about equal, while for  $Co\text{-}CN$ ,  $(Co - B)_{int}\text{-}CN$ , and  $(Co - B)_{non-int}\text{-}CN$ ,  $\Delta G_{H_3O^*}$  is more than  $\Delta G_{H^*}$ . When comparing the  $\eta^{HER}$  and the  $E_{CB}$ , it can be shown that  $CN$ ,  $Co\text{-}CN$ ,  $(Co - B)_{int}\text{-}CN$ , and  $(Co - B)_{non-int}\text{-}CN$  demonstrate the effective use of the B-doped monolayers for hydrogen generation, whereas  $B_{int}\text{-}CN$  and  $B_{non-int}\text{-}CN$  are not found to be appropriate for HER.  $Co\text{-}CN$  has a very low value of  $\eta^{HER}$  among the HER-appropriate monolayers; this value is less than the Pt-loaded  $CN$ 's stated value.

### 3.5 Effectiveness of Co and B over $g\text{-C}_3\text{N}_4$

The following characteristics should be taken into account when designing any material for overall water splitting: (i) significant absorption in the visible energy domain; (ii) appropriate band edges for NHE (iv) an appropriate value of the overpotential ( $\eta^{OER}/\eta^{HER}$ ); (iii) surplus charge carriers on the surface with high mobility and minimal charge carrier recombination. In the current investigation, we functionalized  $CN$  using B-doping, Co-loading, and B-doping and Co-loading combined to construct a material for total water splitting. As can be shown from charge redistribution, substituting B at the C site at either  $C^{bay}$  or  $C^{cor}$  causes a hole in the lattice and increases its affinity to lose its solitary electron to nearby

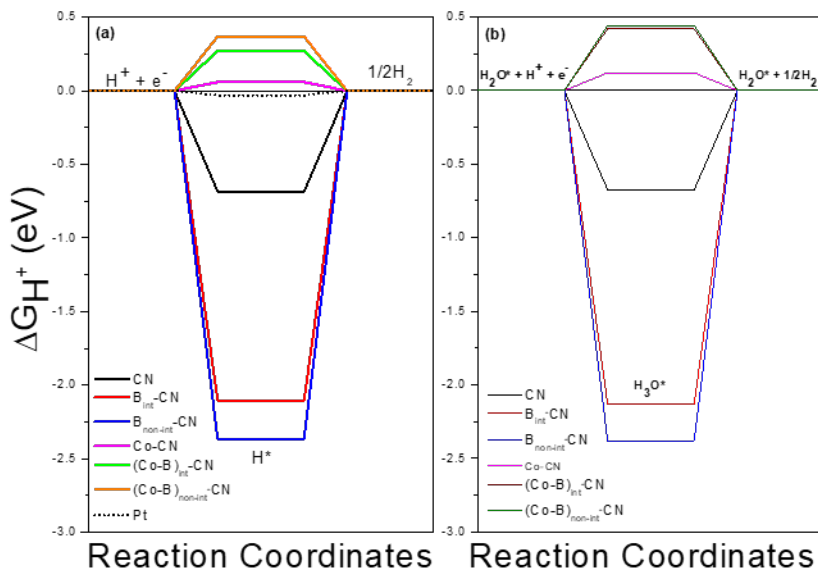


FIGURE 3.6: The Gibbs free energy plot for HER over Pt,  $CN$ ,  $B_{int}\text{-CN}$ ,  $B_{non-int}\text{-CN}$ ,  $Co\text{-CN}$ ,  $(Co-B)_{int}\text{-CN}$ , and  $(Co-B)_{non-int}\text{-CN}$ , using  $H/H_3O$  adsorbate

highly electronegative N. Due to B-N  $p_\pi - p_\pi$  hybridization and the transfer of empty levels to low energy, which reduces the band gap and affects the  $E_{VB}$ , neighboring N plays a significant role in B doping. As a result,  $(Co-B)_{int}\text{-CN}$  does not exhibit OER activity but  $B_{non-int}\text{-CN}$  does. Additionally, as opposed to  $CN$ , B-doping results in a drop in  $\eta^{OER}$  and an increase in hole concentration because of the altered intermediate-to-intermediate interaction. However, the larger value of  $|\eta^{HER}|$  makes simple hydrogen evolution impossible. The presence of partially filled TM (Co) in the lattice increases the electron density due to their affinity to be stable after giving electrons, Co loading provides an electron pair from its 3d orbital which leads to the formation of IB bringing Co-loaded  $CN$  in the visible spectrum while enhancing  $E_{CB}$  for efficient HER,  $p_\pi - d_\pi$  orbital interaction of Co-N facilitate charge redistribution over the  $N^{edge}$  atom making it electron-rich as effective adsorption site for HER. When B-doping and Co-loading are combined,  $CN$ 's  $E_F$  shifts to the center of the forbidden band gap, indicating partial charge compensation.  $(Co-B)_{int}\text{-CN}$  exhibits the maximum absorption

due to the hybridization of the Co-3d and B-2p orbitals, which created impurity states that yield greater absorption when compared to pristine. Furthermore, the negative charge on  $N^{edge}$  atom is seen to be enhanced by the Co-loading in B-doped  $CN$  primarily because of the short [long] range interaction between Co and B in  $(Co - B)_{int}\text{-CN}$  [ $(Co - B)_{non-int}\text{-CN}$ ], which makes the N site active for the effective adsorption of intermediate due to electronegativity difference. Based on the effective mass analysis,  $(Co - B)_{int}\text{-CN}$  exhibits the lowest rate of charge carrier recombination due to the formation of impurity states. These impurity states are thought to act as deep trapping sites, extending the lifetime and availability of photogenerated  $e^- - h^+$  pair for redox reactions. The  $e^- - h^+$  pair that the Co-B combination produces makes it beneficial for both HER and OER. However,  $CN$ 's B site dependence in terms of properties reversed with Co-loading because of a significant Pauling electronegativity difference that depends on the interaction range. In both scenarios, however,  $N^{edge}$  is the best site for adsorption.  $p_\pi - d_\pi$  bonding for Co-B in short-range interaction results from the formation of impurity states and charge redistribution over the plane due to the electron affinity and partially filled Co-3d orbitals, whereas the effect of B in long-range interaction is observed via charge difference on its neighboring N. Thus, an increase in the electronegativity of the  $N^{edge}$  atom results from the development of a channel for charge redistribution, which further enhances other features.  $B_{non-int}\text{-CN}$  and  $Co\text{-CN}$  are the most suitable for OER reaction and HER, respectively, according to thermodynamic analysis.  $(Co - B)_{int}\text{-CN}$  and  $(Co - B)_{non-int}\text{-CN}$  are considered for overall water splitting because the synergistic effect of Co-B interaction is combined with individual doping/loading properties.  $(Co - B)_{int}\text{-CN}$  is an effective photocatalyst for total water splitting if all the influencing factors are taken into account, such as the synergistic impact of impurity states creation, low rate of charge carrier recombination, and low overpotential concerning  $CN$  for both OER and HER.

## 3.6 Conclusion

The pristine  $CN$ ,  $B_{int}\text{-}CN$ ,  $B_{non-int}\text{-}CN$ ,  $Co\text{-}CN$ ,  $(Co - B)_{int}\text{-}CN$ , and  $(Co - B)_{non-int}\text{-}CN$  properties' structural, electronic, and optical characteristics were examined for the application of photocatalytic activity utilizing the h-DFT in the form of an atomic monolayer. B-doping and Co-loading solved the problems of poor charge production and high rate of recombination of  $e^- - h^+$  pair in  $CN$ . In  $CN$ , the partially filled B-2p orbitals aid in the creation of charges and their redistribution.  $(Co - B)_{int}\text{-}CN$  [ $(Co - B)_{non-int}\text{-}CN$ ] shows the formation of IB on Co-loading while sharpening [broadening] impurity states when B interacts with Co with a short [long] range. Sharp impurity states in  $(Co - B)_{int}\text{-}CN$  sharply decreased the rate of  $e^- - h^+$  recombination, increasing the photocatalytic activity's efficiency. An excess negative charge is accumulated on the  $N^{edge}$  atom due to the influence of Co-B short- and long-range interaction and charge redistribution. This alters the adsorption energy of intermediates in HER and OER, modifying overpotential values and improving overall photocatalytic water splitting. For water splitting, we report  $(Co - B)_{int}\text{-}CN$  as a suitable photocatalyst based on overpotential values and band edges analysis.

